

Micro-Raman characterization of Zn-diffused channel waveguides in $\text{Tm}^{3+}:\text{LiNbO}_3$

Marta Quintanilla,^{1,*} Emma Martín Rodríguez,¹ Eugenio Cantelar,¹ Fernando Cussó¹ and Concepción Domingo²

¹Departamento de Física de Materiales (Módulo 04), Universidad Autónoma de Madrid, Avda. Francisco Tomás y Valiente 7. 28049 Madrid, Spain.

²Instituto de Estructura de la Materia, Consejo Superior de Investigaciones Científicas (CSIC), C/ Serrano 121, 28006 Madrid, Spain.

*marta.quintanilla@uam.es

Abstract: In this work micro-Raman scattering experiments have been performed in $\text{LiNbO}_3:\text{Tm}^{3+}$ samples with waveguides fabricated by Zn^{2+} in-diffusion. The results shown that Zn^{2+} ions enter the lattice in Li^+ sites, but also in interstitial positions. This produces a compaction of the lattice close to the surface of the sample, generating the waveguide. It is shown that this region is surrounded by a different area in which the lattice is relaxed to recover the characteristic lattice parameters of $\text{LiNbO}_3:\text{Tm}^{3+}$.

©2010 Optical Society of America

OCIS codes: (300.0300) Spectroscopy; (130.0130) Integrated Optics.

References and links

1. B. K. Das, H. Suche, and W. Sohler, "Single-frequency $\text{Ti}:\text{Er}:\text{LiNbO}_3$ distributed Bragg reflector waveguide laser with thermally fixed photorefractive cavity," *Appl. Phys. B* **73**, 439–442 (2001).
2. A. Guarino, G. Poberaj, D. Rezzonico, R. Degl'innocenti, and P. Günter, "Electro-optically tunable microring resonators in lithium niobate," *Nat. Photonics* **1**(7), 407–410 (2007).
3. J. A. Mackenzie, "Dielectric solid-state planar waveguide lasers: a review," *IEEE J. Quantum Electron.* **13**(3), 626–637 (2007).
4. F. Chen, "Photonic guiding structures in lithium niobate crystals produced by energetic ion beams," *J. Appl. Phys.* **106**(8), 081101 (2009).
5. W. Sohler, H. Hu, R. Ricken, V. Quiring, C. Vannahme, H. Herrmann, D. Büchter, S. Reza, W. Grundkötter, S. Orlov, H. Suche, R. Nouroozi, and Y. Min, "Optical Devices in Lithium Niobate," *Opt. Photon. News* **19**(1), 24–31 (2008).
6. E. Lallier, J. P. Pocholle, M. Papuchon, M. de Micheli, M. J. Li, Q. He, D. B. Ostrowsky, C. Grezes-Besset, and E. P. Pelletier, "Nd:MgO:LiNbO₃ waveguide laser and amplifier," *Opt. Lett.* **15**(12), 682–684 (1990).
7. R. Paschotta, N. Moore, W. A. Clarkson, A. C. Tropper, D. C. Hanna, and G. Mazé, "230 mW of blue light from a thulium-doped upconversion fiber laser," *IEEE J. Quantum Electron.* **3**(4), 1100–1102 (1997).
8. E. Cantelar, J. A. Sanz-García, G. Lifante, F. Cussó, and P. L. Pernas, "Single polarized Tm^{3+} laser in Zn-diffused LiNbO_3 channel waveguides," *Appl. Phys. Lett.* **86**(16), 161119 (2005).
9. A. S. Gouveia-Neto, L. A. Bueno, R. F. do Nascimento, E. A. da Silva, Jr., E. B. da Costa, and V. B. do Nascimento, "White light generation by frequency upconversion in $\text{Tm}^{3+}/\text{Ho}^{3+}/\text{Yb}^{3+}$ -codoped fluorolead germanate glass," *Appl. Phys. Lett.* **91**(9), 091114 (2007).
10. S. Aozasa, H. Masuda, M. Shimizu, and M. Yamada, "Highly efficient S-Band thulium-doped fiber amplifier employing high-thulium-concentration technique," *J. Lightwave Technol.* **25**(8), 2108–2114 (2007).
11. R. Nevado, and G. Lifante, "Low-loss, damage-resistant optical wave-guide in Zn-diffused LiNbO_3 by a two step procedure," *Appl. Phys., A Mater. Sci. Process.* **72**(6), 725–728 (2001).
12. V. Dierolf, and C. Sandmann, "Confocal two-photon emission microscopy: a new approach to waveguide imaging," *J. Lumin.* **102–103**, 201–205 (2003).
13. V. Dierolf, and C. Sandmann, "Inspection of periodically poled waveguide devices by confocal luminescence microscopy," *Appl. Phys. B* **78**(3–4), 363–366 (2004).
14. Y. Zhang, L. Guilbert, and P. Bourson, "Characterization of $\text{Ti}:\text{LiNbO}_3$ waveguides by micro-Raman and luminescence spectroscopy," *Appl. Phys. B* **78**(3–4), 355–361 (2004).
15. A. Harhira, Y. Zhang, P. Bourson, L. Guilbert, M. D. Fontana, M. P. De Micheli, "Raman probing of proton exchange waveguides in lithium niobate," **352**, 153–157 (2007).
16. D. Jaque, E. Cantelar, and G. Lifante, "Lattice micro-modifications induced by Zn diffusion in Nd:LiNbO₃ channel waveguides probed by Nd³⁺ confocal micro-luminescence," *Appl. Phys. B* **88**(2), 201–204 (2007).
17. A. Ródenas, A. H. Nejadmalayeri, D. Jaque, and P. Herman, "Confocal Raman imaging of optical waveguides in LiNbO_3 fabricated by ultrafast high-repetition rate laser-writing," *Opt. Express* **16**(18), 13979–13989 (2008).
18. D. Jaque, F. Chen, and Y. Tan, "Scanning confocal fluorescence imaging and micro-Raman investigations of oxygen implanted channel waveguides in Nd:MgO:LiNbO₃," *Appl. Phys. Lett.* **92**(16), 161908 (2008).

19. M. Quintanilla, E. Martín Rodríguez, E. Cantelar, D. Jaque, J. A. Sanz-García, G. Lifante, and F. Cussó, "Confocal micro-luminescence of Zn-diffused $\text{LiNbO}_3\text{:Tm}^{3+}$ channel waveguides," *J. Lumin.* **129**(12), 1698–1701 (2009).
20. D. Jaque, and F. Chen, "High resolution fluorescence imaging of damage regions in H^+ ion implanted Nd:MgO:LiNbO_3 channel waveguides," *Appl. Phys. Lett.* **94**(1), 011109 (2009).
21. I. Suárez, and G. Lifante, "Detailed study of the two steps for fabricating $\text{LiNbO}_3\text{:Zn}$ optical waveguides," *Appl. Phys. Express* **2**, 022202 (2009).
22. E. Cantelar, G. A. Torchia, J. A. Sanz-García, P. L. Pernas, G. Lifante, and F. Cussó, " Tm^{3+} -doped Zn-diffused LiNbO_3 channel waveguides," *Phys. Scr. T* **118**, 69–71 (2005).
23. V. Caciuc, A. Postnikov, and G. Borstel, "Ab initio structure and zone-center phonons in LiNbO_3 ," *Phys. Rev. B* **61**(13), 8806–8813 (2000).
24. R. Mouras, M. D. Fontana, P. Bourson, and A. V. Postnikov, "Lattice site of Mg ion in LiNbO_3 crystal determined by Raman spectroscopy," *J. Phys. Condens. Matter* **12**(23), 5053–5059 (2000).
25. R. Mouras, P. Bourson, M. D. Fontana, and G. Boulon, "Raman spectroscopy as a probe of rare-earth ions location in LiNbO_3 crystals," *Opt. Commun.* **197**(4-6), 439–444 (2001).
26. C.-T. Chia, M.-L. Sun, M.-L. Hu, J.-Y. Chang, W.-S. Tse, Z.-P. Yang, and H.-H. Chen, "Room temperature A1(TO) and OH- absorption spectra of Zn-doped lithium niobate crystals," *Jpn. J. Appl. Phys.* **42**(Part 1, No. 9B), 6234–6237 (2003).
27. A. Rodenas, L. M. Maestro, M. O. Ramirez, G. A. Torchia, L. Roso, F. Chen, D. Jaque, "Anisotropic lattice changes in femtosecond laser inscribed $\text{Nd}^{3+}\text{:MgO:LiNbO}_3$ optical waveguides," **106**, 013110 (2009).
28. F. Abdi, M. D. Fontana, M. Aillerie, and P. Bourson, "Coexistence of Li and Nb vacancies in the defect structure of pure LiNbO_3 and its relationship to optical properties," *Appl. Phys., A Mater. Sci. Process.* **83**(3), 427–434 (2006).
29. T. S. Chernaya, T. R. Volk, I. A. Verin, and V. I. Simonov, "Threshold Concentrations in Zn-Doped Lithium Niobate Crystals and Their Structural Conditionality," *Crystallogr. Rep.* **53**(4), 573–578 (2008).
30. C.-Y. Chen, J.-C. Chen, and C.-T. Chia, "Growth and optical properties of different compositions of LiNbO_3 single crystal fibers," *Opt. Mater.* **30**(3), 393–398 (2007).
31. V. A. Fedorov, Yu. N. Korkishko, G. Lifante, and F. Cussó, "Optical and structural characterization of Zinc vapour diffused waveguides in LiNbO_3 crystals," *J. Eur. Ceram. Soc.* **19**(6-7), 1563–1567 (1999).
32. A. Jayaraman, and A. A. Ballman, "Effect of pressure on the Raman modes in LiNbO_3 and LiTaO_3 ," *J. Appl. Phys.* **60**(3), 1208–1210 (1986).
33. F. Abdi, M. Aillerie, M. Fontana, P. Bourson, T. Volk, B. Maximov, S. Sulyanov, N. Rubinina, and M. Wöhlecke, "Influence of Zn doping on electrooptical properties and structure parameters of lithium niobate crystals," *Appl. Phys. B* **68**(5), 795–799 (1999).
34. T. S. Chernaya, B. A. Maksimov, T. R. Volk, N. M. Rubinina, and V. I. Simonov, "Zn atoms in lithium niobate and mechanism of their insertion into crystals," *JETP Lett.* **73**(2), 103–106 (2001).
35. L. Zhao, X. Wang, B. Wang, W. Wen, and T.-Y. Zhang, "ZnO-doped LiNbO_3 single crystals studied by X-ray and density measurements," *Appl. Phys. B* **78**(6), 769–774 (2004).
36. D. Xue, and X. He, "Dopant occupancy and structural stability of doped lithium niobate crystals," *Phys. Rev. B* **73**(6), 064113 (2006).
37. A. Lorenzo, H. Jaffrezic, B. Roux, G. Boulon, and J. García-Solé, "Lattice location of rare-earth ions in LiNbO_3 ," *Appl. Phys. Lett.* **67**(25), 3735–3737 (1995).
38. R. Nevado, C. Sada, F. Segato, F. Caccavale, A. Kling, J. C. Soares, E. Cantelar, F. Cussó, and G. Lifante, "Compositional characterization of Zn-diffused lithium niobate waveguides," *Appl. Phys. B* **73**, 555–558 (2001).
39. J. Burghoff, S. Nolte, and A. Tünnermann, "Origins of waveguiding in femtosecond laser-structured LiNbO_3 ," *Appl. Phys., A Mater. Sci. Process.* **89**(1), 127–132 (2007).
40. M. V. Hobden, and J. Warner, "The temperature dependence of the refractive indices of pure lithium niobate," *Phys. Lett.* **22**(3), 243–244 (1966).
41. W. Que, S. Lim, L. Zhang, and X. Yao, "The magnesium diffused layer characteristics of a lithium niobate single crystal with magnesium-ion indiffusion," *Jpn. J. Appl. Phys.* **37**(Part 1, No. 3A), 903–907 (1998).
42. Y. Avrahami, and E. Zolotoyabko, "Diffusion and structural modification of Ti:LiNbO_3 , studied by high-resolution x-ray diffraction," *J. Appl. Phys.* **85**(9), 6447–6452 (1999).

1. Introduction

Nowadays, there is a great interest in the fabrication of optical devices based on locally modified materials to generate channel waveguides. This is due to the advantages that waveguide configuration have in comparison to the bulk material, including the engineering of lasers, amplifiers or other integrated optical devices [1–3].

In that sense, a widely studied material for which several techniques to fabricate waveguides have been developed is LiNbO_3 [4–6]. The reasons for the strong interest in that material are its electro-optical, acousto-optical and non-linear properties, along with the possibility of easily doping it with different atomic species to add new absorption and emission narrow bands in the visible and near-IR region, where the LiNbO_3 matrix is transparent. In that sense, lanthanide ions are among the most studied dopants and particularly

Tm³⁺ is notable due to the wide range of fields in which its emissions are potentially applicable. This is partly thanks to the energetic position of its infrared emissions, interesting in optical communications, surgery or remote sensing, and partly thanks to the resonant character of many transitions that allow efficient up-conversion processes that generates visible frequencies [7–10].

Among the different methods available to create waveguides in LiNbO₃, Zn²⁺ in-diffusion method outstands due to the possibility of confining both polarization modes, ordinary and extraordinary, and because of the especial capacity of Zn²⁺ ions of behaving as photorefractive damage inhibitors, which is of great advantage in laser applications [11]. Unfortunately, a complete characterization of the channel waveguides is hard to achieve. In particular, the question of how Zn²⁺ ions enter the lattice and how this process could modify the properties of the host is not completely answered yet, although the final efficiency of the integrated devices is, to a high extent, dependent on those properties.

Recently, confocal microscopy has emerged as a powerful tool to obtain direct information about the waveguides, as it makes it possible to record spectroscopic information from regions smaller than half squared micron, allowing the opportunity of easily measuring into the waveguide and out of it [12–20]. Combining that method with the sensitivity of Raman scattering to the modifications of the material, it can be used to extract information on the local consequences of the Zn²⁺ incorporation.

In this work, channel waveguides fabricated into LiNbO₃:Tm³⁺ substrates by Zn²⁺ in-diffusion have been studied by means of a confocal microscope used to perform micro-Raman scattering experiments. Through the analysis of the obtained results, information about the waveguide structure and characteristics is obtained.

2. Experimental method

Congruent LiNbO₃ doped with Tm³⁺ ions has been grown by means of the Czochralski technique. The boules have been cut creating substrates, perpendicularly oriented to the c-axis (optical axis), that have been polished up to optical grade. The concentration of thulium ions in the substrates have been found out by X-Ray Fluorescence technique and it has been determined to be 2.4 mol%.

A Zn²⁺ in-diffusion procedure has been applied to fabricate channel waveguides onto the substrates. As a previous step to the diffusion, a SiO₂ layer has been deposited over the substrate and then, by photolithographic techniques, a pattern with 10 μm wide channels has been defined. Once the mask is prepared, the diffusion process is accomplished in a two-step process: first of all, a Zn²⁺ rich layer is created on the surface of the sample by keeping the sample at 500°C during 2 hours in a Zn²⁺ rich atmosphere. Then, the diffusion of Zn²⁺ ions from this layer into the sample is performed by means of an annealing stage in open atmosphere at 850 °C for 4 h. Details on the fabrication procedure can be found elsewhere [11, 21].

After that treatment, M-line measurements at the He-Ne laser wavelength ($\lambda = 632.8$ nm) were performed to characterize the waveguides. Using the obtained data a depth of the waveguide of 6.5 μm was estimated, and maximum index changes of 0.18% and 0.10% for n_e and n_o , respectively, were obtained [22].

The confocal experiments have been achieved using an Olympus BX41 optical microscope adequately modified with a Jobin-Yvon module to transform it in a confocal microscope. As excitation source the main blue line of a CW argon laser has been used (488.0 nm). The laser beam is focalized onto the sample by a microscope objective (50x, N.A. = 0.75) to a spot of around 0.3 μm of diameter. The Raman signal emitted by the sample is recovered by the same microscope objective, and separated from the excitation beam using an interferential narrow band filter (notch filter). The signal is then focused in a fiber-coupled high-resolution spectrometer (SPEX 500M) and detected by means of a CCD camera.

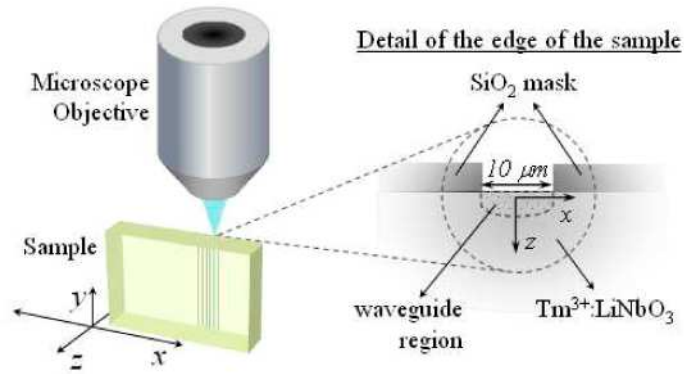


Fig. 1. Excitation scheme and position of the sample in the confocal microscope. On the right hand side of the figure a detail of the sample shows the reference system defined in this work.

The excited region over the sample is optically selected by means of a camera coupled to the microscope. The sample is placed over a motorized XY stage that can be precisely moved with $0.1\ \mu\text{m}$ spatial resolution, changing and commanding by this way the excitation spot location. In this work, the sample movement is described according to x and z axes, depicted in Fig. 1. Taking into account that the measurements have been carried out on the edge of the sample, and hence, over a section of the channel waveguide, it can be seen in the figure that the x -axis identifies the direction parallel to the surface of the sample, while z -axis identifies the perpendicular direction, i.e. the depth of the waveguide. Finally, the origin of the axes is located in the middle of the silica-mask opening, at the surface of the sample.

3. Results and discussion

In Fig. 2, two Raman spectra of $\text{LiNbO}_3:\text{Tm}^{3+}$, excited and detected along the y -axis, are shown (see Fig. 1 for the excitation axis). Those spectra have been measured in a location on the sample around $20\ \mu\text{m}$ away from the sample edge, distance enough to assure that they are taken outside the waveguide region, where no Zn^{2+} ions are present and hence the spectra correspond to bulk $\text{LiNbO}_3:\text{Tm}^{3+}$.

Figure 2(a) corresponds to un-polarized measurements, while Fig. 2(b) corresponds to a spectrum measured under $Y(ZZ)\bar{Y}$ configuration. The assignment of the phonons made by Caciuc et al. [23] has been applied to label the Raman modes that can be clearly identified in the figure. It is possible to extract detailed information from all these peaks from the spectrum in Fig. 2(a). However, some other modes are strongly overlapped and it is not possible to accurately analyze them using that spectrum. This is the case of $A_1(\text{TO}_1)$ and $A_1(\text{TO}_2)$ modes, which are particularly relevant due to their high sensitivity to the presence of doping ions in the lattice [24–26]. Nevertheless, that information can be clarified by measuring under $Y(ZZ)\bar{Y}$ polarization. It can be seen in Fig. 2(b) that, by means of this configuration, due to the corresponding selection rules three main modes prevail, including $A_1(\text{TO}_1)$ and $A_1(\text{TO}_2)$.

In order to study the effects of Zn^{2+} -ions within the waveguide region, polarized and non-polarized Raman spectra have been recorded along a horizontal trajectory parallel to the surface of the sample at one micron depth ($z = -1\ \mu\text{m}$) where, according to the optical characterization performed for this sample [22], the modes are confined. The spectra have been recorded at $0.7\ \mu\text{m}$ intervals, covering a distance of $36\ \mu\text{m}$ (from $x = -18\ \mu\text{m}$ to $x = 18\ \mu\text{m}$) substantially longer than the mask opening that has $10\ \mu\text{m}$ width (see Fig. 1), in order to assure that the extreme regions belong to unperturbed bulk material.

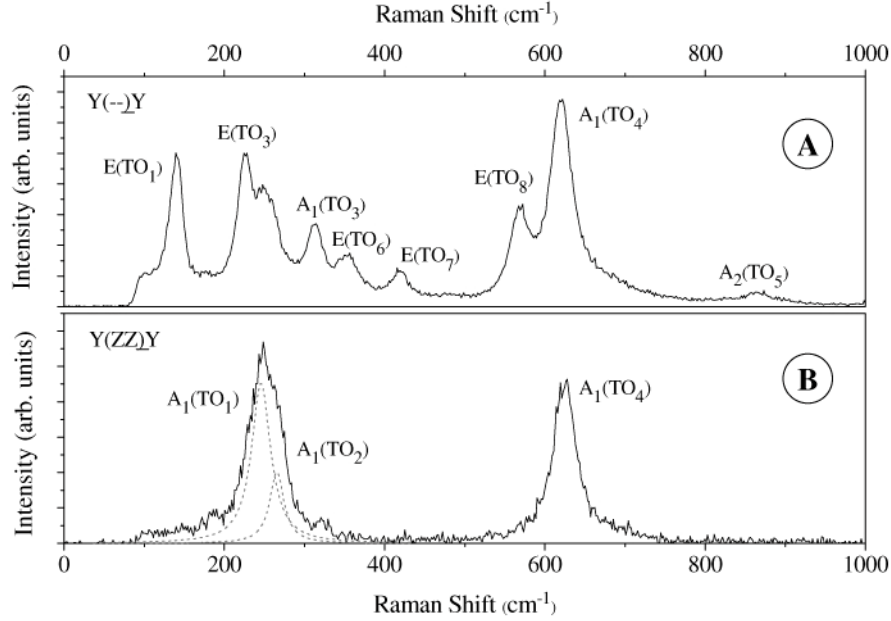


Fig. 2. Raman spectra of $\text{LiNbO}_3:\text{Tm}^{3+}$ without any polarization (a), and under $Y(ZZ)\bar{Y}$ configuration (b). The modes have been labeled according to [23]. The dashed lines in (b) are depicted to clarify $A_1(\text{TO}_1)$ and $A_1(\text{TO}_2)$ modes position..

All the data have been fitted to Lorentzian-shaped curves (like the dashed lines in Fig. 2(b)) to obtain the corresponding value for the bandwidth and Raman shift of the different modes. The obtained results, relative to the bulk values, are presented in Fig. 3. In the upper part of the figure the Raman shift is represented while the lower part corresponds to the bandwidth variation. On the left hand side, data from un-polarized spectra are plotted, while those from polarized spectra are represented on the right hand side (Figs. b).

The results are summarized in Table 1, where the wavenumber shift ($\Delta p = p_{\text{wg}} - p_{\text{bulk}}$) and bandwidth variation ($\Delta w = w_{\text{wg}} - w_{\text{bulk}}$) for each mode in the centre of the waveguide are given. The value has been calculated from the average position of the data between $-3 \mu\text{m} < x < 3 \mu\text{m}$, and therefore, the errors given come from the deviation of the data in this range. A short description of each mode, provided by the eigenvector calculation reported in [23], is also included.

A first inspection of the experimental data of Fig. 3 and Table 1 reveals that all the modes are affected by the incorporation of Zn^{2+} ions, although their sensitivity is different. The distortion has a bell shaped dependence, symmetrically spread around the central position of the silica-mask opening ($x = 0 \mu\text{m}$). The distortion exhibits a flattened maximum central section, which extends roughly through the mask opening region ($-5 \mu\text{m} < x < 5 \mu\text{m}$), and then it gradually decreases as the measuring location moves away from the center. As it can be observed in Fig. 3 both, the peak position and bandwidth, do not recover the characteristic values of bulk $\text{LiNbO}_3:\text{Tm}^{3+}$ until the probe point has been moved substantially farther ($x \approx \pm 13 \mu\text{m}$) than the mask opening limits ($x \approx \pm 5 \mu\text{m}$). This result indicates a lateral spread of the diffused ions, extending beyond the silica mask opening, and resulting in a waveguide width of $26 \mu\text{m}$ at one micron depth. This result is comparable to those observed by other techniques in Zn^{2+} and Ti-diffused LiNbO_3 waveguides [14, 16].

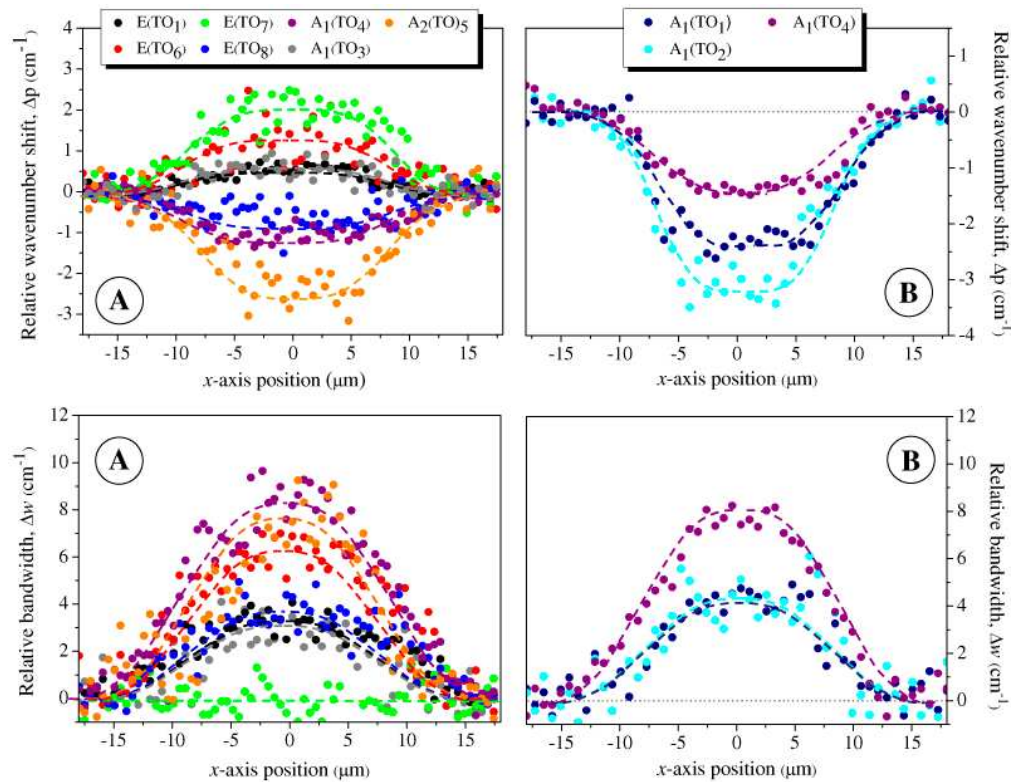


Fig. 3. Wavenumber shift (up) and bandwidth (down) of all the measured Raman modes in the non-polarized configuration (a) and under Y(ZZ)Y configuration (b). All the results are displayed relative to the bulk values. The lines have been drawn to guide the eye.

As it is apparent from Fig. 3, the half-width, Δw , of the modes is always increased inside the waveguide; however the changes observed in the peak wavenumber position, Δp , can be either positive or negative, depending on the particular mode. This fact is consistent with different sensitivities of the modes to diverse perturbations of the lattice [25, 27], and it will be discussed later on.

The frequency of a phonon and the shift from its position in the bulk material can be associated to the ionic masses and the chemical bonds between the ions involved in this particular vibration. For that reason this is a sensitive magnitude to the presence of defects in the sites related to each Raman mode. Consequently, the examination of the Raman modes characteristics can be used to obtain information about the modifications induced in the material by the incorporation of dopants such as Zn^{2+} ions.

In fact, previous theoretical and experimental works have demonstrated that $A_1(\text{TO}_2)$ phonon can be used to detect changes associated to Li^+ sites [23, 26, 28]. That possibility is related to the distinctive movement associated to the mode, namely a relatively large displacement of the ions in Li^+ sites along the Z-axis (ferroelectric axis) against the ions in Nb^{5+} sites, which are only slightly affected. Supporting that, previous results have shown that, $A_1(\text{TO}_2)$ phonon is very sensitive to the introduction of Zn^{2+} or Mg^{2+} ions when they are incorporated during the crystal growth, since they both enter the lattice predominantly in Li^+ sites [24, 26].

Similarly, an inspection of the data obtained in the present work reveals that it is $A_1(\text{TO}_2)$ the mode that suffers the highest wavenumber shift within the waveguide region. This shift takes place towards lower wavenumbers, also in good agreement with the results of Mouras et al. [24], who attributed that shift to an increase of the effective mass of the mode due to the substitution of Li^+ ions by doping ions. Therefore, the present results indicate that during the

fabrication process of the waveguides, Li^+ lattice sites become occupied by the in-diffused Zn^{2+} ions, in a similar way as it happens when the Zn^{2+} incorporation takes place during the crystal growth.

Table 1. Summary of the results obtained for all the analyzed Raman modes and a short description of the main characteristics of each one, following the theoretical results of Caciuc et al. [23].

Phonon	Description	Δp (cm^{-1})	Δw (cm^{-1})
$\text{E}(\text{TO}_1)$	Nb^{5+}/O vibrations in the XY plane	0.62 ± 0.08	4.0 ± 0.5
$\text{E}(\text{TO}_6)$	Displacement of the ions mainly in Li^+ sites but also in Nb^{5+} sites in the XY plane. Slight deformation of the oxygen octahedron	1.5 ± 0.3	6.8 ± 0.9
$\text{E}(\text{TO}_7)$	Movement in both sites, Nb^{5+} and Li^+ , in the XY plane.	2.0 ± 0.3	0 ± 1
$\text{E}(\text{TO}_8)$	Deformation of the oxygen octahedron.	-0.8 ± 0.2	4.0 ± 0.5
$\text{A}_1(\text{TO}_1)$	Movement of the ions in Nb^{5+} sites along the Z-axis direction and against the oxygen plane.	-2.5 ± 0.5	4 ± 1
$\text{A}_1(\text{TO}_2)$	Displacement of ions in Nb^{5+} and Li^+ sites along the Z-axis. Oxygen remains motionless.	-3.2 ± 0.5	4.0 ± 0.5
$\text{A}_1(\text{TO}_3)$	Deformation of the oxygen octahedron in the XY plane.	0.7 ± 0.3	4.0 ± 0.5
$\text{A}_1(\text{TO}_4)$	Deformation of the oxygen octahedron in the XY plane.	-1.5 ± 0.2	8.2 ± 0.7
$\text{A}_2(\text{TO}_5)$	Deformation of the oxygen octahedron.	-2.5 ± 0.5	8 ± 2

This interpretation is also consistent with the changes observed in $\text{A}_1(\text{TO}_4)$ mode. It has been previously shown that its width is highly sensitive to the introduction of doping ions in Li^+ sites [26]. As it can be seen, that result is in good agreement with the data shown in Fig. 3 and Table 1, where it can be verified that this mode exhibits the highest distortion in that sense, supporting the former conclusion.

Besides, the agreement between the results obtained in this work and those presented in works focused on the incorporation of doping ions during the crystal growth is not complete, since a narrowing of $\text{A}_1(\text{TO}_1)$ is found in samples fabricated by this last technique [24,26]. Instead, from the inspection of Table 1 it is apparent that in the present case the modes appear to be substantially wider in the region of diffusion than in the $\text{LiNbO}_3:\text{TM}^{3+}$ substrate. Generally, the width of a phonon mode can be correlated to the degree of disorder of the crystal lattice in the surroundings of the sites associated to each particular mode and hence, it can be used to estimate the number of defects in the lattice [28–30]. Therefore, the narrowing of a Raman mode observed in crystals where doping ions have been incorporated during the crystal growth, has been attributed to an increase in the order of the lattice, mainly associated to the disappearance of the intrinsic defects associated to Li^+ sites in LiNbO_3 [24–26].

This reasoning would imply that in the present case, where a general broadening of the Raman spectra is observed, the incorporation of the ions could not be just limited to the mentioned lattice sites, but to different locations that would contribute to the deformation of the lattice. Along this line, it has been previously suggested from X-ray diffraction data [31] that the incorporation of Zn^{2+} by a diffusion method takes also place in interstitial positions, predominantly near a basal (oxygen) plane, which would create a deformation of the lattice consistent with the present observations.

An additional way to extract information about the lattice modifications induced within the waveguide region is to analyze the changes associated to $E(\text{TO}_6)$ phonon. It has been demonstrated by Jayaraman et al. [32] that this phonon can be used as a good probe for the detection of pressure changes in the lattice, as it shows the highest sensitivity to this kind of perturbations. According to their work, a shift of this mode towards higher wavenumbers is associated to an increase of the pressure, and hence to a reduction of the volume of the unit cell, while a shift towards lower wavenumbers signifies a reduction of the pressure, i.e. an increase of the volume. As it can be observed, the experimental results given in Fig. 3 reveal a positive displacement of the mode in the wavenumber scale, indicating a pressure increase within the waveguide region, also consistent with the presence of interstitial Zn^{2+} ions.

In order to explore how this lattice distortion could affect the overall structure of the waveguide and nearby regions, a 2D map showing the values of the magnitudes under study is considered. Those maps are shown in Fig. 4, where the pressure probe $E(\text{TO}_6)$ phonon, along with the maps of two other modes, $E(\text{TO}_1)$ and $A_1(\text{TO}_4)$, are drawn. The maps have been obtained by measuring a set of spectra, acquired at $0.7 \mu\text{m}$ length intervals, in the area between $-18 \mu\text{m} < x < 18 \mu\text{m}$ and $0 \mu\text{m} < z < -15 \mu\text{m}$, covering therefore the whole region of diffusion and beyond.

On the left hand side of the figure, the bandwidth results are depicted, while on the right hand side the Raman shift of the modes can be seen. In all the maps, the geometry is consistent with that shown in Fig. 1, as it is indicated by the axes. The surface of the sample is located on the upper part of the figures, being the SiO_2 mask out of the images, while bulk $\text{LiNbO}_3:\text{Tm}^{3+}$ is on the base and lateral limits of the maps. As it is shown in the scale bar on the left, the lighter colors correspond to higher wavenumbers, while the darker shades represent lower wavenumbers. The color scale has been normalized in every map separately to allow the clear view of all the induced modifications.

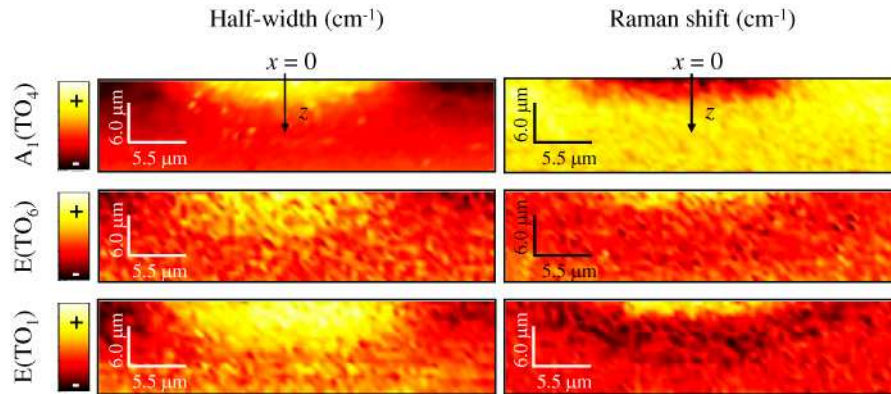


Fig. 4. 2D maps of three of the measured maps: $A_1(\text{TO}_4)$, $E(\text{TO}_6)$ and $E(\text{TO}_1)$. The results of the half-width of each mode are displayed on the left, while the Raman shift is on the right. For the sake of clarity, in the maps of $A_1(\text{TO}_4)$ the reference axes are represented.

In the maps of those modes two different regions are apparent. It can be appreciated that close to the surface of the sample the mode is shifted towards higher energies. This area gets down to a depth of around $4 \mu\text{m}$, and is surrounded by a differentiated belt-shaped region in which the modifications go towards lower energies down to a depth of around $10 \mu\text{m}$. From Table 1, it becomes clear that the biggest changes are induced in $E(\text{TO}_6)$ phonon, although $E(\text{TO}_1)$ seems to be clearer in the maps due to a lower dispersion of the results and the previously mentioned normalization of the color scale.

As it has been already said, $E(\text{TO}_6)$ mode is directly related to the pressure in the material. For that reason, the pattern observed in the Raman shift map can be translated to a pressure landscape: the area close to the surface, in which the mode is shifted towards higher wavenumbers, corresponds to a higher pressure region and therefore a contraction of the

lattice can be assumed. On the contrary, in the deeper belt-shaped region the pressure is lower than in bulk $\text{LiNbO}_3:\text{Tm}^{3+}$, implying an expansion of the lattice.

This spatial variation can be visualized following the Raman shift of $\text{E}(\text{TO}_6)$ mode along a line $-\xi\text{O}\xi$, represented in the inset of Fig. 5, that diagonally crosses the sample from the down left corner of the map ($-\xi$) up to the origin of the axes (O), on the surface of the sample, and then back down to the right corner of the map (ξ). As it can be observed in Fig. 5, the evolution of the relative Raman shift (Δp) along this line draws a symmetrical curve with extreme values corresponding to the bulk material, a central high peak ($\Delta p = 1.6 \text{ cm}^{-1}$) related to the region close to the sample surface and two lateral regions with negative Raman shift ($\Delta p = -0.45 \text{ cm}^{-1}$) associated to the belt-shaped region, which is crossed twice along the mentioned line $-\xi\text{O}\xi$.

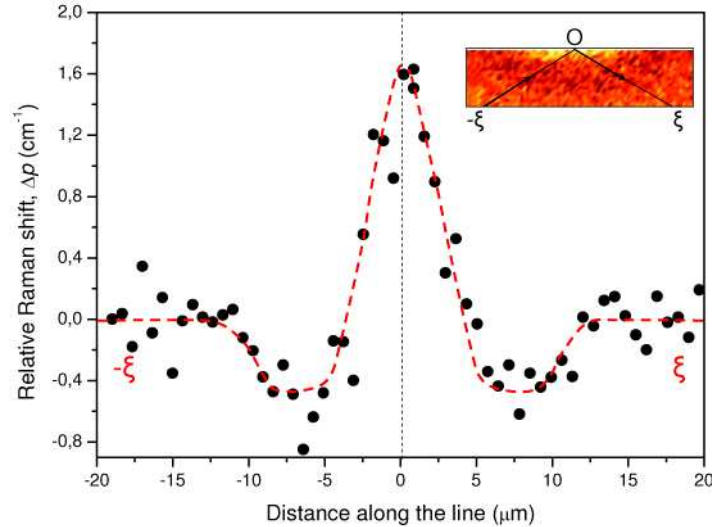


Fig. 5. Spatial dependence of the relative Raman shift (Δp) of $\text{E}(\text{TO}_6)$ phonon along the $-\xi\text{O}\xi$ line, represented in the inset.

In order to understand all the above described results, it should be considered that according to the most commonly accepted model, when Zn^{2+} ions are incorporated to LiNbO_3 during the crystal growth, they enter the lattice in Li^+ sites, eliminating the so-called antisites (Nb^{5+} ions in Li^+ sites) [33–35]. In the present case, it must be also taken into account that the situation is slightly different, as the original material is already doped with Tm^{3+} ions and Zn^{2+} ions are introduced after the crystal growth by a diffusion process.

The previous doping with Tm^{3+} ions implies that the structure of defects is different than in pure LiNbO_3 since lanthanide ions enter the lattice mainly occupying Li^+ sites [36, 37], and hence their presence would imply that the quantity of antisites has been lowered. Nevertheless, the incorporation of Zn^{2+} ions is energetically favored in Li^+ sites and the Raman data indicate that indeed, such incorporation takes place. Additionally, as it has been formerly mentioned, it seems that interstitial occupancy may play also an important role in the incorporation of Zn^{2+} ions due to the use of a diffusion method and to the lower availability of energetically favored Li^+ sites.

As a result of these processes the diffused area close to the surface of the sample, in which according to SIMS measurements a high concentration of Zn^{2+} ions can be found [38], becomes compressed. The high compaction of the lattice in this area would be then surrounded by a low pressure region in which the lattice relaxes and recovers the usual $\text{LiNbO}_3:\text{Tm}^{3+}$ characteristics, giving rise to the belt-shaped region that can be observed in Figs. 4 and 5.

It has been recently proved that one of the most important effects that produces optical waveguiding in LiNbO_3 arises from the refractive index changes associated to stress of the

lattice through the elasto-optic effect [39]. This implies that the above mentioned compression and dilatation of the lattice can be associated to refractive index changes. The magnitude of these changes can be estimated through the Clausius-Mossotti equation that, in its differential form, is expressed as:

$$\frac{\Delta V}{V} = -\frac{6n}{(n^2 - 1)(n^2 + 2)} \Delta n \approx -0.5 \Delta n \quad (1)$$

where a refractive index value of $n \approx 2.2$ has been used in the last step [40].

According to that relationship, a lattice compression involves a positive increment of the refractive index value. This is consistent with the fact that the light is confined in the region close to the surface of the sample where, as it has been formerly said, a higher Zn^{2+} content is found. Subsequently, the expanded surrounding area would be associated to some refractive index reduction, contributing to the localization of the guided modes. This kind of behaviour has been already observed in femtosecond-laser inscribed waveguides, where refractive index profiles for different irradiation geometries have been successfully reproduced from the LiNbO_3 elasto-optic tensors [39].

Considering that the experimental refractive index changes in Zn^{2+} in-diffused waveguides are of the order of 2×10^{-3} , a volume change around $\Delta V/V \approx 10^{-3}$ can be estimated from Eq. (1). It has to be mentioned that the elasto-optic effect may not be the only one contributing to the refractive index changes, and other possibilities, such as the modification of the spontaneous polarization could be also contributing to the final refractive index of the waveguide. Despite of that, the obtained value for $\Delta V/V$ is consistent with the results presented in previous works to characterize the modifications created in LiNbO_3 by the diffusion of different metals [41, 42], and therefore, this agreement suggests an important contribution of the elasto-optic effect to the refractive index modification, as it has been previously postulated regarding femtosecond laser inscribed waveguides [39].

5. Conclusions

Confocal microscope experiments have been used to study the Raman spectra of Zn^{2+} in-diffused channel waveguides, since by that technique it is possible to measure into the waveguide and out of it. The observed modifications generated in the Raman modes can be explained considering the perturbations generated in the unit cell of the crystal due to the introduction of Zn^{2+} by a diffusion method.

The obtained results suggest that through this method Zn^{2+} ions enter the lattice both in Li^+ sites and in interstitial positions, in contrast with the behavior observed in different works in which the ions are introduced during the crystal growth. This would generate several changes in the shape and size of the unit cell, creating the waveguide.

The representation of 2-D maps in which the Raman modes variations are depicted, reveals two different regions of distortion in the sample. In one of them, closer to the surface of the sample and related to the area with a higher Zn^{2+} concentration, a compaction of the material can be deduced. This region is also associated to a refractive index increase that allows the possibility of confining the light. Surrounding this region it has been observed a low-pressure belt-shaped area, necessary to accommodate the overall lattice relaxation and to recover the bulk characteristics after the contraction created in the more superficial region.

Acknowledgements

This work has been partially supported by Comunidad de Madrid under project MICROSERES-CM (S-0505/TIC/0191). M. Quintanilla is supported by FPU program from Ministerio de Ciencia e Innovación (AP2005-0763). The authors would like to thank also Profs. D. Jaque and G. Lifante for their assistance within the experimental setup and helpful discussions in the interpretation of the data.